Transactions of Tianjin University (2022) 28:163–173
https://doi.org/10.1007/s12209-022-00320-3

RESEARCH ARTICLE

Manipulating Spin Polarization of Defected Co_3O_4 for Highly Efficient Electrocatalysis

Yue Li[1] · Tianzuo Wang[1] · Muhammad Asim[1] · Lun Pan[1,2,3,4] · Rongrong Zhang[1] · Zhen-Feng Huang[1,2,3,4] · Zhichao Chen[1] · Chengxiang Shi[1] · Xiangwen Zhang[1,2,3,4] · Ji-Jun Zou[1,2,3,4]

Received: 11 April 2022 / Revised: 19 April 2022 / Accepted: 24 April 2022 / Published online: 15 June 2022

Abstract

Electrocatalytic water splitting is limited by kinetics-sluggish oxygen evolution, in which the activity of catalysts depends on their electronic structure. However, the influence of electron spin polarization on catalytic activity is ambiguous. Herein, we successfully regulate the spin polarization of Co_3O_4 catalysts by tuning the concentration of cobalt defects from 0.8 to 14.5%. X-ray absorption spectroscopy spectra and density functional theory calculations confirm that the spin polarization of Co_3O_4 is positively correlated with the concentration of cobalt defects. Importantly, the enhanced spin polarization can increase hydroxyl group absorption to significantly decrease the Gibbs free energy change value of the OER rate-determining step and regulate the spin polarization of oxygen species through a spin electron-exchange process to easily produce triplet-state O_2, which can obviously increase electrocatalytic OER activity. In specific, Co_3O_4-50 with 14.5% cobalt defects exhibits the highest spin polarization and shows the best normalized OER activity. This work provides an important strategy to increase the water splitting activity of electrocatalysts via the rational regulation of electron spin polarization.

Keywords Co_3O_4 · Cobalt defect · Oxygen evolution reaction · Spin polarization · Transition metals · Water splitting

Introduction

Electrocatalytic water splitting by renewable energies has been considered to be a promising way to produce hydrogen [1, 2], which is a sustainable and green energy to effectively solve the urgent problems, like exhaustion of energy, excessive emissions of carbon oxide and so on [3–5]. The theoretical voltage of electrolytic water is 1.23 V but a larger cell voltage is usually required, due to the energy loss derived from intrinsic electrode reaction, ohmic-drop, mass transfer, etc. The kinetically sluggish four-electron oxygen evolution reaction (OER) is the main reason of the high overpotential [6, 7]. Transition metal (hydro)oxides, especially Fe, Co and Ni compounds, deliver outstanding OER activity and have been considered to be promising substitutes for precious metal oxides (RuO_2 and IrO_2), because of their low cost, high reserve and the facile modulation of the electron structures [8, 9]. Actually, the electron spin state translates from spin singlet reactants (OH^-/H_2O) to spin triplet products O_2 are required in both adsorbate evolution mechanism (AEM) and lattice oxygen mechanism (LOM) with electrons extracted in a specific spin direction [10], which puts high demands for the electron spin structure of electrocatalysts [11]. Catalysts with optimized electron spin structures could show promising OER performance.

In recent years, Yang et al. [12] found that OER activity depends on the electron spin state of transition metal ions, providing a new perspective on spin state regulation to improve OER activity. Meanwhile, previous studies

Yue Li and Tianzuo Wang have contributed equally to this work.

✉ Lun Pan
panlun76@tju.edu.cn

✉ Ji-Jun Zou
jj_zou@tju.edu.cn

1 Key Laboratory for Green Chemical Technology of the Ministry of Education, School of Chemical Engineering and Technology, Tianjin University, Tianjin 300072, China

2 Haihe Laboratory of Sustainable Chemical Transformations, Tianjin 300192, China

3 Zhejiang Institute of Tianjin University, Ningbo 315201, Zhejiang, China

4 Collaborative Innovative Center of Chemical Science and Engineering (Tianjin), Tianjin 300072, China

found that chiral-induced spin selectivity can promote triple oxygen production by inducing the electron parallel spin arrangement of reactants (•OH radicals) [13–16]. Furthermore, applying an external magnetic field to magnetic transition metal catalysts can adjust the spin direction of electrons to make them parallel and form triplet oxygen quickly, thus reducing the energy barrier of OER [17–21]. Xu et al. [18, 22, 23] also studied the spin polarization of transition metal oxide catalysts to enhance water oxidation, such as ferromagnetic $CoFe_2O_4$ as a spin polarizer under a constant magnetic field, reconstructed oxyhydroxide layer on ferromagnetic $Co_{3-x}Fe_xO_4$ with the spin pinning effect, and spin-polarized channels of antiferromagnetic inverse spinel oxide $LiCoVO_4$. However, the influence of the inherent spin-polarized surface structure of electrocatalysts on spin-related OER steps remains unclear.

Recently, our group has constructed metal-defected ZnO [24], TiO_2 [25, 26], Mn_3O_4 [27], and Co_3O_4 [28] via simple solvothermal treatment followed by thermal calcination in air, with the key process of encapsulation of $–CH_2–OH$ groups on M–O–M skeleton, and found that different glycerol dosages can quantitatively regulate metal defect content. In addition, the presence of metal defects can manipulate the electron spin polarization of catalysts and improve photocatalytic water splitting [26].

Transition metal oxide Co_3O_4 is a promising OER non-noble metal electrolyte with mixed Co^{2+} and Co^{3+} species [29, 30]. In the present work, we prepared a series of Co-defected Co_3O_4 with varied contents of Co defects and explored the effect of electron spin polarization regulated by metal defect content on OER activity. The enhanced spin polarization can increase the hydroxyl group adsorption to significantly decrease the ΔG value of the OER rate-determining step and regulate the spin polarization of adsorbed oxygen species through a spin electron-exchange process to easily produce triplet-state O_2, which obviously increases the electrocatalytic OER activity. This work serves as a guide to regulating the spin polarization of electrocatalysts for highly efficient water splitting.

Experimental Section

Materials

Glycerol and anhydrous ethanol were all purchased from Tianjin Yuanli Chemical Co., Ltd., China. Cobalt(II) acetate tetrahydrate was obtained from Shanghai J&K Chemical, China. Potassium hydroxide was obtained from Shanghai Macklin Biochemical Co., Ltd., China. Shenzhen Nafion was purchased from DuPont Company, China, and Milli-Q ultrapure water (> 18.2 MΩ·cm) was used in all experiments.

Preparation of Co_3O_4 with Different Co Defects

Cobalt acetate (2 g), x mL ($x = 0$, 5, 10, 30, 50) of glycerol, and (80-x) mL of absolute ethanol were mixed in a 100-mL Teflon-lined autoclave, magnetically stirred for 1 h, and then hydrothermally reacted at 180 °C for 2 h in an oven. The obtained purple powders were dried at 60 °C for 12 h. Then, the cobalt glycerolate precursor was obtained (labeled as C-x). Then, C-x was calcined at 300 °C in a muffle furnace for 2 h with a heating rate of 5 °C/min to obtain Co_3O_4 catalysts with different Co defects, which are named Co_3O_4-x.

Characterizations

X-ray diffraction (XRD) patterns were recorded with a Panalytical X'Pert Pro X-ray diffractometer equipped with Cu Kα radiation at 40 kV and 40 mA at a scanning rate of 5°/min. Thermogravimetric (TG) analysis was tested on an HCT-1 integrated thermal analyzer with a rate of 5 °C/min under air flow. Fourier transform infrared (FT-IR) spectra were obtained on a BioRad FTS 6000 spectrometer. All samples were pressed into thin sheets mixed with KBr. Transmission electron microscopy (TEM) was conducted on JEM-F200 with a field-emission gun operating at 200 kV. Spherical aberration-corrected images were obtained using scanning TEM (FEITitan) at 300 kV. X-ray photoelectron spectroscopy was performed with a PHI-1600 X-ray photoelectron spectroscope equipped with Al Kα radiation, and the binding energy was calibrated with the C 1s peak (284.8 eV) of contamination carbon. Inductively coupled plasma optical emission spectrometry (ICP-OES) was conducted using VISTA-MPX. Electron paramagnetic resonance was performed using JESFA200 of JEOL. X-ray absorption spectroscopy (XAS) was conducted on the beam line BL02B02 of the Shanghai Synchrotron Radiation Facility.

Calculation

Density functional theory (DFT) calculations were carried out with the VASP code using the projected augmented wave method [31]. The generalized gradient approximation (GGA-PBE) was used for the exchange–correlation functional [32, 33]. Given that spinel Co_3O_4 are strongly correlated systems, the static electronic correlations were considered in the GGA + U method [33], where the effective U values of 3.2 eV and 0 eV were chosen for Co and O, respectively [34]. The D3 method was used to modify the van der Waals effect. For bulk calculations, we used a plane-wave cutoff of 520 eV and a k-point mesh of $9 \times 9 \times 8$ and performed full relaxation of the unit cell and the internal parameters until the residual forces were less than 0.01 eV/Å. The (110)

surfaces of Co_3O_4 were simulated using slabs containing four-layer and two-layer terminations. The slabs were separated by a vacuum layer with thickness of 20 Å to eliminate the interaction between the slab and its periodic images along the *z*-direction. For surface calculations, we used a plane-wave cutoff of 520 eV and Gamma *k*-point meshes of $3\times3\times1$ and $9\times9\times1$ for structural optimization and electronic characteristics, respectively. The internal positions for the slabs were relaxed until the residual forces were less than 0.01 eV/Å. In this work, an implicit solvent model was selected to treat water solvents, where water molecules were simulated as continuous electrolytes.

Electrochemical Measurements of OER Properties

An electrochemical performance test was carried out on the IVIUMSTAT using a three-electrode system with a 3-mm glassy carbon electrode as the working electrode, Hg/HgO as the reference electrode, and a graphite rod as the counter electrode in 1 mol/L KOH electrolyte. The Co_3O_4 dispersion solution was dip-coated on a glass carbon electrode to prepare a working electrode. Linear sweep voltammetry (LSV) was tested with a scan rate of 5 mV/s from 1.1 to 1.8 V (vs. RHE). Electrochemical impedance spectroscopy (EIS) was conducted over the frequency range of 10^{-1}–10^5 Hz with 10 mV sinusoidal ac perturbation at 1.6 V (vs. RHE).

Results and Discussion

Crystal Structure of Co_3O_4-*x*

XRD patterns of the cobalt glycerolate precursor are shown in Fig. 1a. C-5 and C-10 show the diffraction peak at $2\theta = 10.6°$, which represents the metal-based glycerolate [26]. With the increase in glycerol content, the peak at $2\theta = 10.6°$ gradually becomes sharper and splits into three peaks for C-30 and C-50. This result indicates that the crystallization of C-*x* increases with increasing glycerol content, which is beneficial to forming metal defects in the corresponding oxides after thermal calcination [25, 26]. The TG curves in Fig. 1b show that the cobalt glycerolate precursors (C-*x*) are oxidized completely to form CO_2 and H_2O by oxygen before 300 °C and that no more weight loss occurs when the temperature is further increased. Thus, 300 °C is selected as the calcination temperature to convert glycerol cobalt to cobalt oxides. Moreover, the weight loss percentage of C-*x* increases gradually with the rise in *x* value, which also demonstrates that the precursor crystallization increases from C-5 to C-50. The FT-IR spectra (Fig. 1c) show that the peaks at approximately 1400 and 2800 cm^{-1}, which respectively represent the bending and stretching vibrations of C–H bonds [35, 36], have changed obviously from the single peak of C-5 and C-10 to the splitting peaks of C-30 and C-50. This result indicates that

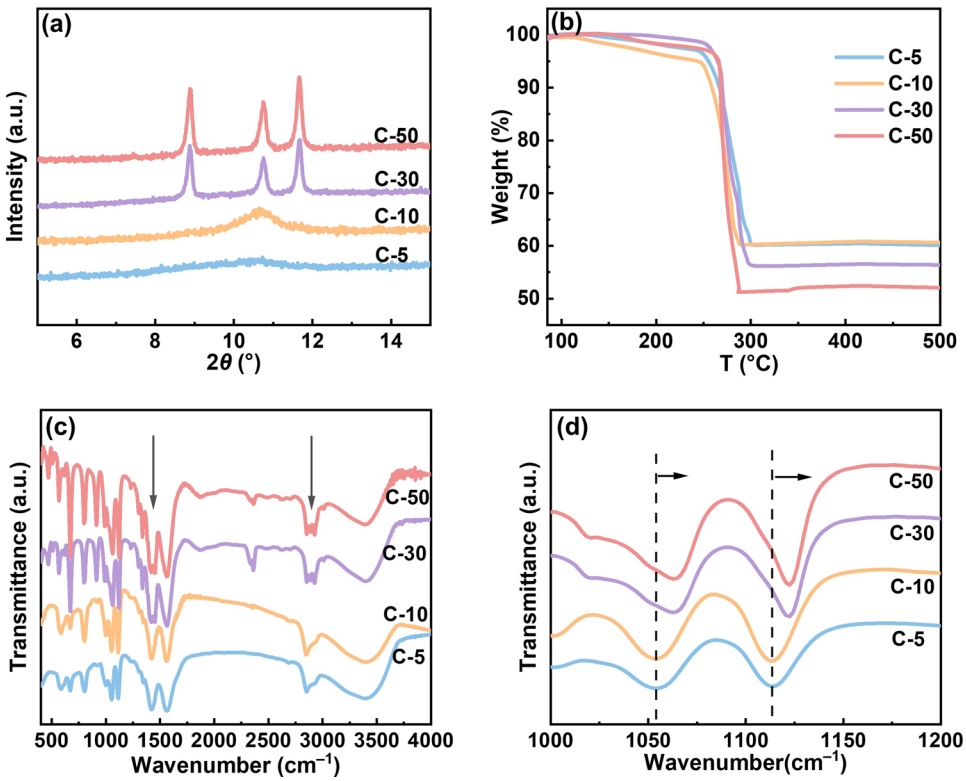

Fig. 1 **a** XRD patterns, **b** TG curves, **c** FT-IR spectra, and **d** enlarged FT-IR spectra of C-*x* precursors

more glycerol groups are present in the precursor structure than those in the C-5 and C-10. As shown in Fig. 1d, the peaks (for C–O stretching vibration bands of glycerol) at 1114 and 1054 cm^{-1} shift to higher wavenumbers with the *x* value increasing from 5 to 30, which indicates that more Co atoms are coordinated with glycerol groups [35, 37]. In addition, all products obtained after the calcination of the precursors only show two peaks at approximately 570 and 665 cm^{-1} (Fig. S1), which refer to the IR absorption of Co_3O_4 with a stretching vibration of Co–O bonds, indicating that Co_3O_4 is produced with the glycerol completely removed [38].

Cobalt Defects in Co_3O_4-*x*

The thermal calcination of C-*x* precursors produces defected Co_3O_4-*x* samples. From the XRD patterns (Fig. 2a), all Co_3O_4-*x* samples show the same diffraction peaks, which correspond to the cubic Fd3 m Co_3O_4 (JCPDSNo. 42-1467). The TEM images display that the Co_3O_4-*x* samples show similar nanoparticle morphologies with a crystal size of ca. 12–14 nm (Fig. S2a–e). In the HR-TEM images (Fig. 2b–f), the lattice fringes of the Co_3O_4-*x* samples correspond to the characteristic planes of Co_3O_4 [39]. The above results confirm that the obtained Co_3O_4-*x* samples show the pure Co_3O_4 phase without other impurities.

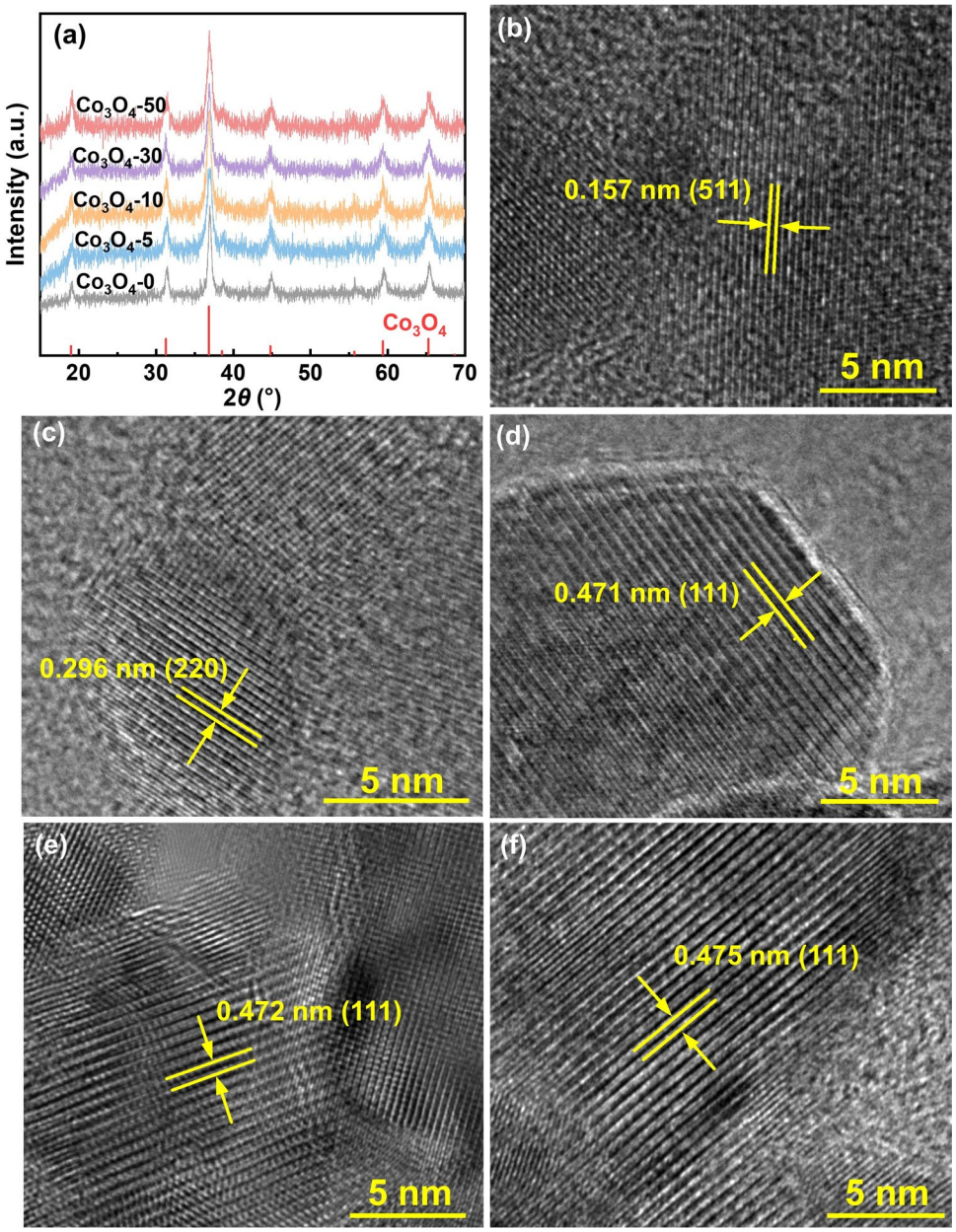

Fig. 2 **a** XRD patterns and HR-TEM images of **b** Co_3O_4-0, **c** Co_3O_4-5, **d** Co_3O_4-10, **e** Co_3O_4-30, and **f** Co_3O_4-50

As shown in Fig. 3a, the intensity distribution of the spherical aberration-corrected STEM image along the selected area suggests the existence of vacancies in the surface lattice, which should be the cobalt defect [40, 41].

ICP-OES of the Co_3O_4-x samples was conducted to characterize the Co defect content in Co_3O_4. The results are shown in Fig. 3b. Almost no defects are found in Co_3O_4-0, while Co defects are introduced to the Co_3O_4-x samples with $x > 0$. The atomic content of Co defects in the Co_3O_4-x samples increases from 0.80 to 14.5% when x is increased from 5 to 50. However, the Co defect content slightly changes from Co_3O_4-40 to Co_3O_4-50, indicating that the glycerol dosage almost reaches the limit to further increase the Co defect content.

In the Co 2p spectra of the Co_3O_4-x samples (Fig. S3a), two typical peaks at the binding energies of 795.4 and 780.2 eV refer to Co $2p_{3/2}$ and Co $2p_{1/2}$, respectively. The Co $2p_{3/2}$ and Co $2p_{1/2}$ peaks can be fitted to be Co^{3+} and Co^{2+} sub-peaks, respectively, and the Co^{3+}/Co^{2+} ratio of the Co_3O_4-x samples is calculated by the area of all sub-peaks (Fig. S3b–f) [42]. As shown in Fig. 3c, the Co^{3+}/Co^{2+} ratio increases gradually from 2.027 for Co_3O_4-0 to 3.030 for Co_3O_4-50, which is caused by the increase in Co^{2+} defect content because the formation energy of Co^{2+} is lower than that of Co^{3+} [28].

Cobalt-Defect-Dependent Spin Polarization of Co_3O_4-x

The above results show that the initial dosage of glycerol can change the crystal structure of the cobalt glycerolate precursor and further control the cobalt defect concentration in an oxygen-rich environment, which can provide a possibility to manipulate the electron spin polarization of Co_3O_4 catalysts. X-ray absorption fine structure spectroscopy was employed to investigate the electronic properties of cobalt atoms in the Co_3O_4-x samples. As shown in Fig. S4 (and Fig. 3d), all samples display two peaks at approximately 783.3 and 797.4 eV, which can be attributed to Co_3O_4 L_3 and L_2 peaks and correspond to the spin–orbit coupling splitting of the initial $2p$ states into $2p_{3/2}$ (L_3) and $2p_{1/2}$ (L_2), which directly refer to the electrons in spin-up (spin quantum number $m_s = +1/2$) and spin-down ($m_s = -1/2$) states, respectively [43]. The intensity of L_2 peaks becomes higher from Co_3O_4-0 to Co_3O_4-50, with L_3 peaks maintaining a similar intensity, which clearly demonstrates that spin polarization (Co_3O_4-0 without metal defects is used as a benchmark) increases with increasing cobalt defect content [26].

Electrocatalytic Activity of Co_3O_4-x Samples

A three-electrode system in 1 mol/L KOH electrolyte was used to test the OER performance of Co_3O_4 catalysts. The polarization curves obtained by LSV are shown in Fig. 4a.

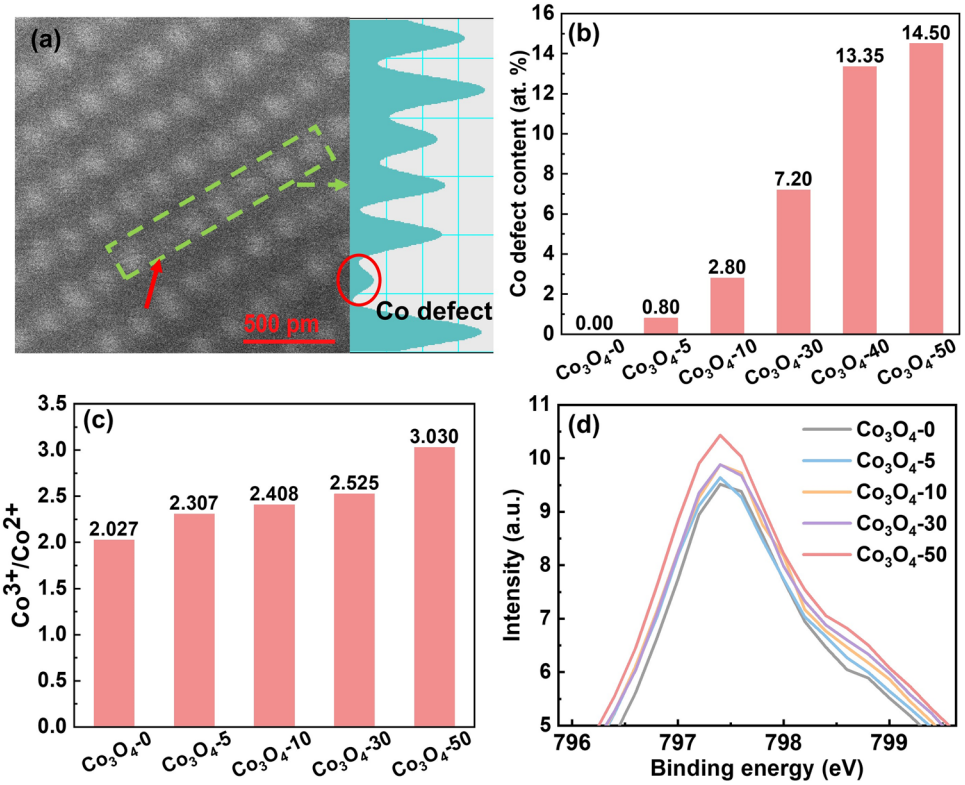

Fig. 3 **a** Spherical aberration-corrected STEM image of Co_3O_4-50 and the intensity profiles along the selected regions, **b** Co defect content (at.%), **c** ratio of $Co^{3+}/Co.^{2+}$, and **d** high-resolution L_2 XAS spectra of Co_3O_4-x samples

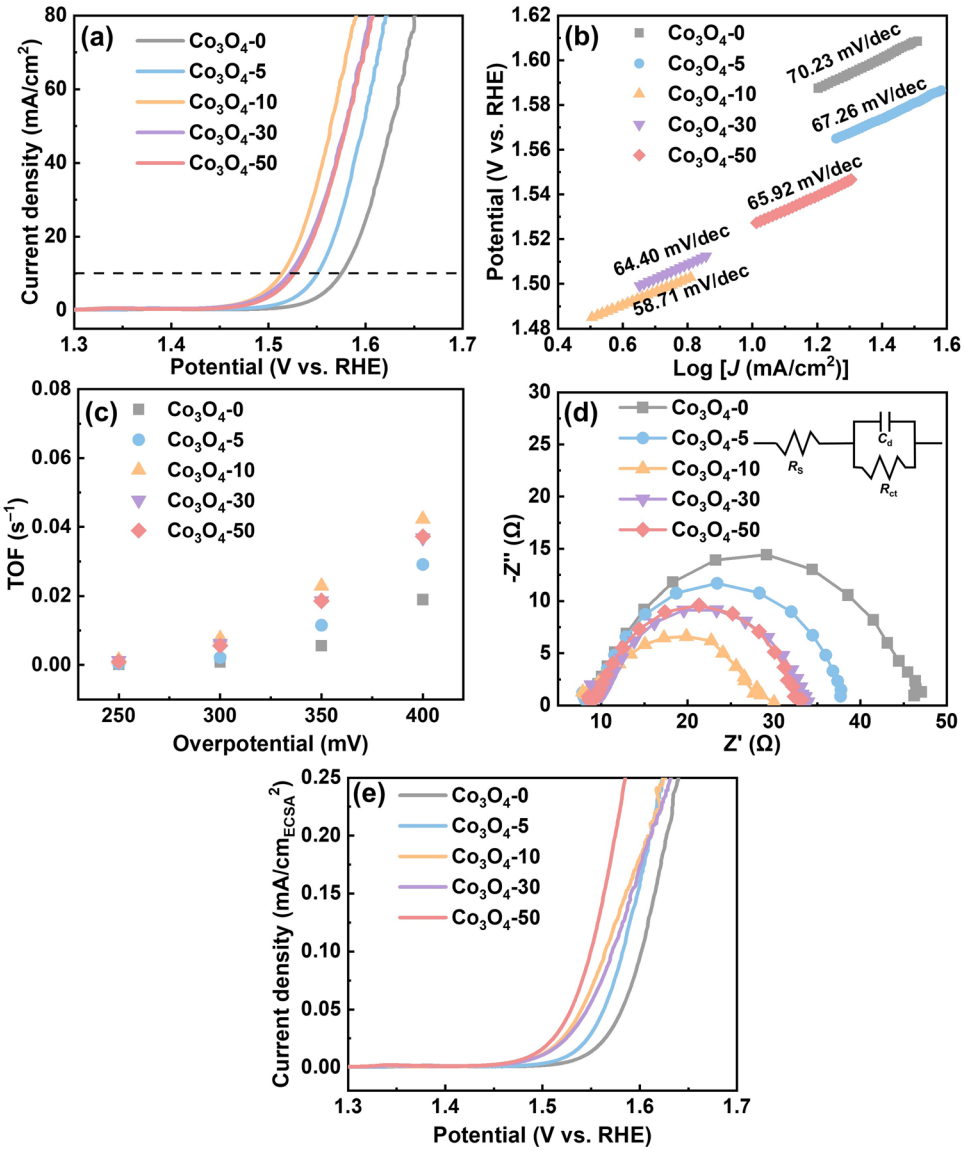

Fig. 4 **a** Polarization curves, **b** Tafel plots, **c** TOF plots, **d** electrochemical impedance spectroscopy (EIS), and **e** normalized OER activity of Co_3O_4-*x* samples

The overpotential at 10 mA/cm^2 of the Co_3O_4-*x* samples decreases rapidly and then slightly decreases as the *x* value is increased from 0 to 10 and then to 50, and Co_3O_4-10 shows the best electrocatalytic OER performance (with an overpotential of 284 mV at 10 mA/cm^2). This result suggests that Co defects can effectively improve OER performance and that appropriate defect content is favorable to obtain the highest OER activity. As shown in Fig. 4b, the Tafel slope of Co_3O_4-10 is 58.71 mV/dec, which is less than those of Co_3O_4-0 (70.23 mV/dec), Co_3O_4-5 (67.26 mV/dec), Co_3O_4-30 (64.40 mV/dec), and Co_3O_4-50 (65.92 mV/dec), indicating its fast electrocatalytic kinetics (smaller potential change results in greater current density growth).

A rotating disk test was carried out to investigate the average number of electron transfers in OER, and the results are shown in Fig. S5 and Table S1. All Co_3O_4-*x* samples perform four-electron reaction processes to generate oxygen molecules, with a Faradaic efficiency of nearly 100% for O_2 generation [28, 44]. Turnover frequency (TOF) can reflect the intrinsic activity of catalysts [45]. As shown in Fig. 4c, Co_3O_4-10 obtains the highest TOF value (i.e., 0.023 s^{-1} at an overpotential of 350 mV), followed by Co_3O_4-30, Co_3O_4-50, Co_3O_4-5, and Co_3O_4-0.

Electrical conductivity affects OER activity, which can be tested through EIS [46]. As shown in Fig. 4d, the Co-defected Co_3O_4-*x* samples show much lower charge transfer resistance (R_{ct}: Co_3O_4-5, 37.7 Ω; Co_3O_4-10, 30.0 Ω; Co_3O_4-30, 33.9 Ω; Co_3O_4-50, 33.2 Ω) than Co_3O_4-0 (47.1 Ω), indicating that Co defects can promote the electrical conductivity. Then, the electrochemical active surface area (ECSA) is calculated according to the double-electric layer theory by CV curves (Fig. S6) [47]. Pristine Co_3O_4 shows a low ECSA of 18.17 cm^2, and the introduction of Co defects obviously increases the active catalytic area, with the ECSA values of 23.67 cm^2 for Co_3O_4-5

and 35.67 cm^2 for Co_3O_4-10. However, further increasing the x value of Co_3O_4-x leads to gradual crystal aggregation (Fig. S7), resulting in decreased ECSA values, i.e., 30.50 cm^2 for Co_3O_4-30 and 15.67 cm^2 for Co_3O_4-50. The LSV curves in Fig. S8 show that Co_3O_4-50 is stable during the 50-cycle test, with the Co/O ratio almost unchanged (Table S2). In addition, the stability of defective OER catalysts has been verified by Pan and Xie et al. [48, 49]. Our group also found that the OER activity of Co-defect Co_3O_4 is stable [28].

LSV activity was normalized using ECSA to eliminate the influence of crystal aggregation on the electrochemical activity of the Co_3O_4-x samples [50]. As shown in Fig. 4e, the normalized OER activity of the Co_3O_4-x samples increases gradually with the x value raising from 0 to 50, and Co_3O_4-50 shows the best normalized electrocatalytic activity, which indicates that the catalytic OER activity is closely correlated to the concentration of cobalt vacancies (and spin polarization) in Co_3O_4.

Correlation Between Spin Polarization and Electrocatalytic Activity

The electrocatalytic OER in alkaline media usually has a four-step electron transfer reaction pathway [51]:

$$OH^- + {}^* \rightarrow {}^*OH + e^- \quad (1)$$

$$OH^- + {}^*OH \rightarrow {}^*O + H_2O + e^- \quad (2)$$

$$OH^- + {}^*O \rightarrow {}^*OOH + e^- \quad (3)$$

$$OH^- + {}^*OOH \rightarrow {}^* + O_2 + H_2O + e^- \quad (4)$$

The superscript * indicates the active metal site or the adsorbed intermediate, and each step has only one electron transfer. Importantly, the conversion of singlet-state reactant H_2O (or OH^-) to triplet-state product O_2 molecules must follow spin conservation, which is the main reason for the high energy barrier of OER [21].

Only the •OH adsorbed on active sites with parallel electron spin can produce triplet O_2. Opposite spin directions of surface •OH species produce singlet-state H_2O_2 or singlet-state O_2 (ca. 1 eV higher than that of triplet O_2 [52]), which inhibits electrocatalytic OER activity. Therefore, the enhancement of •OH spin polarization is the key to accelerating OER kinetics [16]. As shown in Fig. 3d and Fig. 4e, the normalized OER activity of the Co_3O_4-x samples is consistent with their electron spin polarization from XAS. With the highest spin polarization, Co_3O_4-50 shows the best normalized activity, which is much higher than that of pristine Co_3O_4-0.

DFT calculations were performed to reveal the electronic structure of Co_3O_4 and Co-defected $Co_{2.625}O_4$, and the calculation models (Fig. 5a, b) are based on Co_3O_4-0 and Co_3O_4-50. As shown in Fig. 5c, the band gap of pristine Co_3O_4 is 1.2 eV (similar to a previous report [28]), which greatly reduces to nearly 0 eV for $Co_{2.625}O_4$ (Fig. 5d). The electron wave function of Co and O atoms shows larger overlap areas in $Co_{2.625}O_4$ than that in pristine Co_3O_4, indicating that the Co–O bond hybridization of the defected catalyst is stronger than that of the pristine one, which is beneficial to

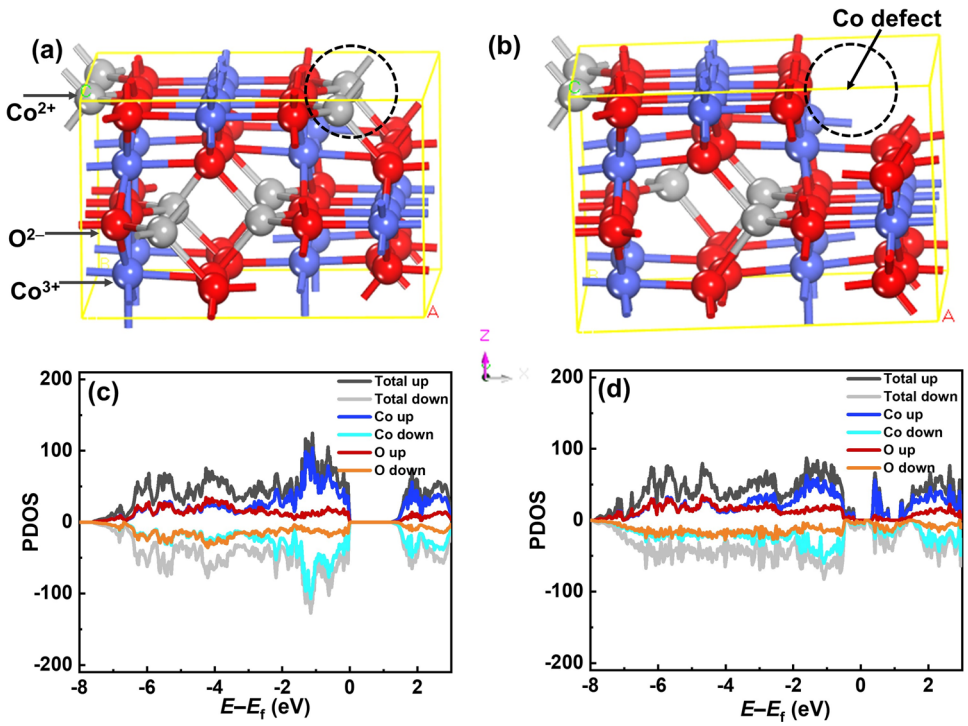

Fig. 5 Calculation models and projected density of states (PDOS) of **a**, **c** Co_3O_4 and **b**, **d** Co defected $Co_{3-m}O_4$ ($Co_{2.625}O_4$)

the charge transfer [28, 53], as confirmed via EIS in Fig. 4d. Moreover, the projected density of states (PDOS) of the spin-down state near the Fermi level of $Co_{2.625}O_4$ is much higher than that of the spin-up state. This result indicates that Co defects polarize the electron spin.

The specific spin polarizability of Co_3O_4 and $Co_{2.625}O_4$ was calculated, as shown in Fig. 6a (detailed calculation is provided in SI). Pristine Co_3O_4 shows very weak spin polarization, whereas the introduction of cobalt vacancies results in strong spin polarization for $Co_{2.625}O_4$ (corresponding to the PDOS analysis and the XAS results), which is mainly contributed by the electrons at the Co_1 (nearby the cobalt vacancy) 3d orbital. In addition, the adjacent oxygen of Co_1 shows a relatively high spin polarization caused by the overlap of the Co 3*d*-O 2*p* orbital [18, 23]. As shown in Fig. 6b, the normalized OER activity of the Co_3O_4-*x* samples positively correlates with the calculated or/and experimental spin polarization, which confirms that electron spin polarization determines the catalytic conversion of singlet-state oxygen species to triplet O_2.

Then, the Gibbs free energy of OER at 1.23 V (vs. RHE) for Co_3O_4 and $Co_{2.625}O_4$ was calculated (Fig. 7a). The OER rate-determining step (RDS) for pristine Co_3O_4 is the first step with a high energy barrier of 0.788 eV, which can be significantly reduced to 0.095 eV by the Co defects ($Co_{2.625}O_4$), and the RDS changes to the third step with a low ΔG value of 0.255 eV (Table S3), indicating that the spin-polarized active sites are more dynamically favorable to OER. As shown in Fig. 7b, $Co_{2.625}O_4$ shows stronger *OH adsorption than the pristine Co_3O_4, which helps significantly decrease the ΔG value of OERRDS (the first step). Moreover, the modulation of surface oxygen species adsorption by Co defects can decrease the maximum reaction energy barrier of Co_3O_4-catalyzed OER (Fig. 7a), which increases OER performance.

The Co defects induce the obvious electron spin polarization of Co-defected Co_3O_4 (Figs. 3d, 6), which can regulate the spin polarization of surface-adsorbed oxygen species. As shown in Fig. 8, for pristine Co_3O_4, the hydroxyl group with O in a random spin direction (e.g., spin-up direction) can be adsorbed on surface Co^{3+} sites, and the proton and electron of –OH are removed to form M–O(↑). After the adsorption of *OH, M–O(↑) –O(↓) –H can be obtained (the calculated results are shown in Fig. S9). For the different spin directions of two oxygen atoms, steps 3 and 4 show a higher energy barrier (0.549 eV, Fig. 7a) to obtain O–O with the same spin direction for the triplet O_2 production. By contrast, the spin-polarized Co^{3+} active sites of Co-defected Co_3O_4 regulate the spin polarization of oxygen species through a spin electron-exchange process [54], i.e., M–O(↓), M–O(↓) –O(↓) –H (Fig. 8, Fig. S9), which can easily produce triplet-state O_2

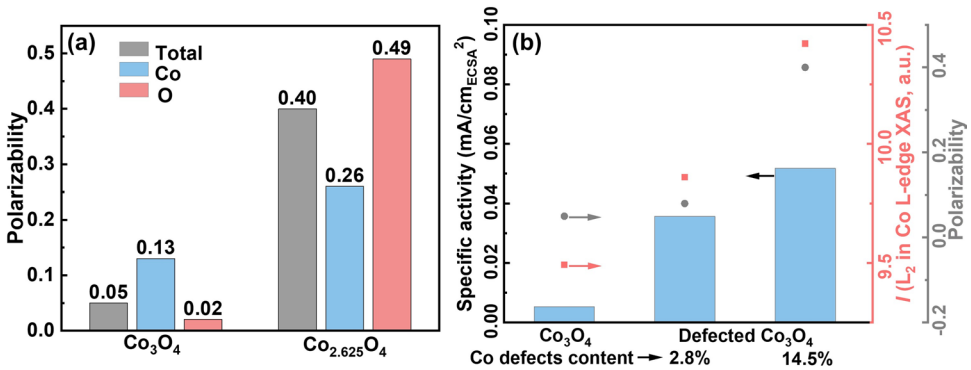

Fig. 6 **a** Spin polarizability of Co_3O_4 and $Co_{2.625}O_4$ (calculated with the energy interval of [E_f-0.2 eV, E_f]). **b** Correlation among spin polarizability, XAS Co L-edge intensity, and normalized OER activity at 1.53 V versus RHE of Co_3O_4 and defected Co_3O_4

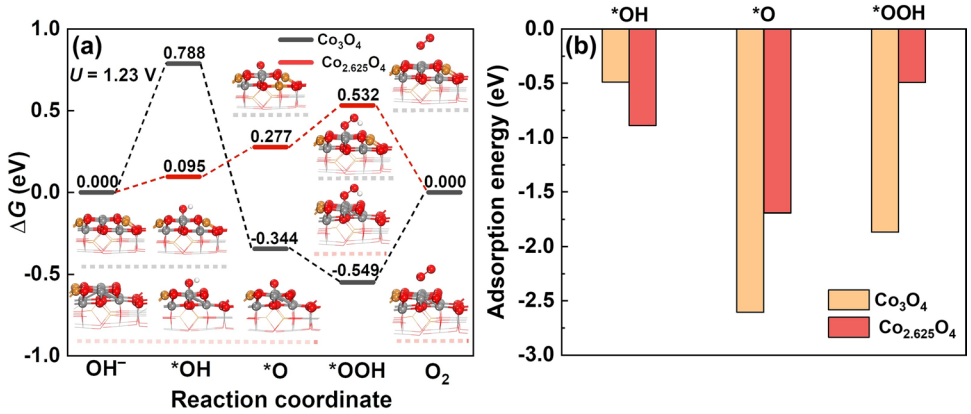

Fig. 7 **a** Calculated free energy diagram of OER at $U = 1.23$ V (vs. RHE) and **b** adsorption energies of oxygen species on Co_3O_4 and $Co_{2.625}O_4$

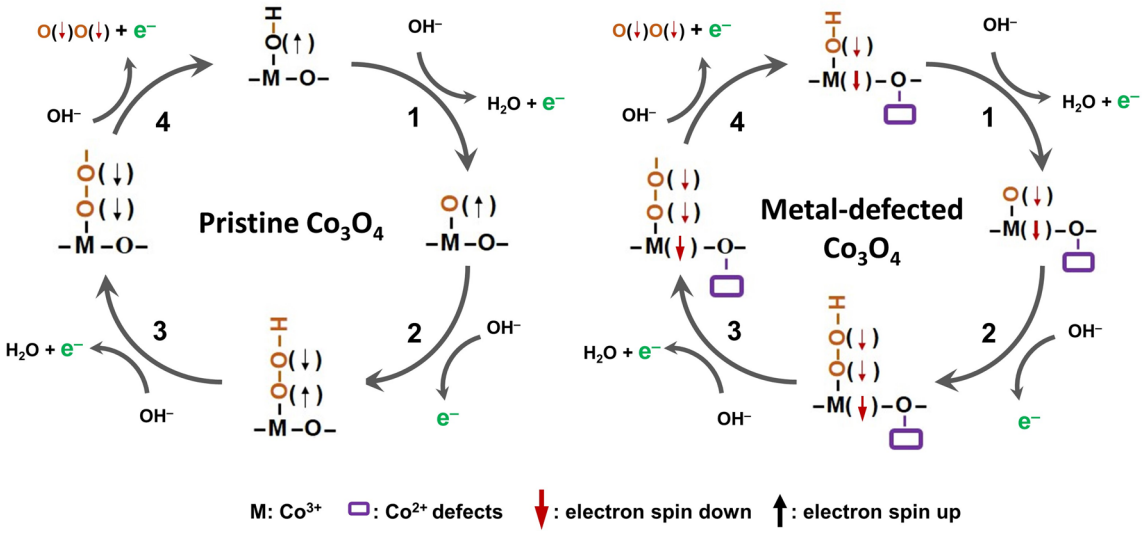

Fig. 8 Proposed OER mechanisms catalyzed by pristine and metal-defected Co_3O_4

($\Delta G_{O_2} - \Delta G_{*OOH} = -0.532\,eV$) and considerably improve OER performance.

Conclusion

We regulated the spin polarization of Co_3O_4 by adjusting the concentration of Co defects and found that the increase in spin polarization positively affects electrocatalytic OER activity. The enhanced spin polarization of Co-defected Co_3O_4 can increase the initial hydroxyl group adsorption to significantly decrease the ΔG value of OER RDS and regulate the spin polarization of oxygen species through a spin electron-exchange process to easily produce triplet-state O_2, which can obviously increase electrocatalytic OER activity. In specific, Co_3O_4-50 with ca. 14.5% cobalt defect exhibits the largest spin polarization and shows the best normalized OER activity. This work provides an important strategy to increase the water splitting activity of electrocatalysts via the rational regulation of electron spin polarization.

Supplementary Information The online version contains supplementary material available at https://doi.org/10.1007/s12209-022-00320-3.

Acknowledgements The authors appreciate the financial support from the National Natural Science Foundation of China (Nos. 21978200 and 22161142002) and the Haihe Laboratory of Sustainable Chemical Transformations (CYZC202103).

Declarations

Conflict of interest The authors declare that they have no conflict of interest.

References

1. Roger I, Shipman MA, Symes MD (2017) Earth-abundant catalysts for electrochemical and photoelectrochemical water splitting. Nat Rev Chem 1:3
2. Li X, Zhao LL, Yu JY et al (2020) Water splitting: from electrode to green energy system. Nanomicro Lett 12(1):131
3. Chu S, Majumdar A (2012) Opportunities and challenges for a sustainable energy future. Nature 488(7411):294–303
4. Yang DX, Zhu QG, Han BX (2020) Electroreduction of CO_2 in ionic liquid-based electrolytes. Innovation (NY) 1(1):100016
5. Chen JM (2021) Carbon neutrality: toward a sustainable future. Innovation (NY) 2(3):100127
6. Retuerto M, Pascual L, Calle-Vallejo F et al (2019) Na-doped ruthenium perovskite electrocatalysts with improved oxygen evolution activity and durability in acidic media. Nat Commun 10(1):2041
7. Bhanja P, Mohanty B, Patra AK et al (2019) IrO_2 and Pt doped mesoporous SnO_2 nanospheres as efficient electrocatalysts for the facile OER and HER. ChemCatChem 11(1):583–592
8. Liu G, Wu Y, Yao R et al (2021) Amorphous iron-nickel phosphide nanocone arrays as efficient bifunctional electrodes for overall water splitting. Green Energy Environ 6(4):496–505
9. Pei XY, Zhang YF, Mu Y et al (2022) Cobalt oxide decorated three-dimensional amorphous carbon/cobalt silicate composite

derived from bamboo leaves enables the enhanced oxygen evolution reaction. Chem Eng Sci 251:117490
10. Lim T, Niemantsverdriet JW, Gracia J (2016) Layered antiferromagnetic ordering in the most active perovskite catalysts for the oxygen evolution reaction. ChemCatChem 8(18):2968–2974
11. Li XN, Cheng ZX, Wang XL (2021) Understanding the mechanism of the oxygen evolution reaction with consideration of spin. Electrochem Energy Rev 4(1):136–145
12. Suntivich J, May KJ, Gasteiger HA et al (2011) A perovskite oxide optimized for oxygen evolution catalysis from molecular orbital principles. Science 334(6061):1383–1385
13. Naaman R, Waldeck DH (2012) Chiral-induced spin selectivity effect. J Phys Chem Lett 3(16):2178–2187
14. Mtangi W, Kiran V, Fontanesi C et al (2015) Role of the electron spin polarization in water splitting. J Phys Chem Lett 6(24):4916–4922
15. Mtangi W, Tassinari F, Vankayala K et al (2017) Control of electrons' spin eliminates hydrogen peroxide formation during water splitting. J Am Chem Soc 139(7):2794–2798
16. Zhang WY, Banerjee-Ghosh K, Tassinari F et al (2018) Enhanced electrochemical water splitting with chiral molecule-coated Fe_3O_4 nanoparticles. ACS Energy Lett 3(10):2308–2313
17. Liao ZM, Li YD, Xu J et al (2006) Spin-filter effect in magnetite nanowire. Nano Lett 6(6):1087–1091
18. Ren X, Wu TZ, Sun YM et al (2021) Spin-polarized oxygen evolution reaction under magnetic field. Nat Commun 12(1):2608
19. Zhang YY, Liang C, Wu J et al (2020) Recent advances in magnetic field-enhanced electrocatalysis. ACS Appl Energy Mater 3(11):10303–10316
20. Yan JH, Wang Y, Zhang YY et al (2021) Direct magnetic reinforcement of electrocatalytic ORR/OER with electromagnetic induction of magnetic catalysts. Adv Mater 33(5):e2007525
21. Garcés-Pineda FA, Blasco-Ahicart M, Nieto-Castro D et al (2019) Direct magnetic enhancement of electrocatalytic water oxidation in alkaline media. Nat Energy 4(6):519–525
22. Wu TZ, Ren X, Sun YM et al (2021) Spin pinning effect to reconstructed oxyhydroxide layer on ferromagnetic oxides for enhanced water oxidation. Nat Commun 12(1):3634
23. Chen RR, Sun YM, Ong SJH et al (2020) Antiferromagnetic inverse spinel oxide $LiCoVO_4$ with spin-polarized channels for water oxidation. Adv Mater 32(10):e1907976
24. Pan L, Wang SB, Mi WB et al (2014) Undoped ZnO abundant with metal vacancies. Nano Energy 9:71–79
25. Wang SB, Pan L, Song JJ et al (2015) Titanium-defected undoped anatase TiO_2 with p-type conductivity, room-temperature ferromagnetism, and remarkable photocatalytic performance. J Am Chem Soc 137(8):2975–2983
26. Pan L, Ai MH, Huang CY et al (2020) Manipulating spin polarization of titanium dioxide for efficient photocatalysis. Nat Commun 11(1):418
27. Li K, Zhang RR, Gao RJ et al (2019) Metal-defected spinel $Mn_xCo_{3-x}O_4$ with octahedral Mn-enriched surface for highly efficient oxygen reduction reaction. Appl Catal B Environ 244:536–545
28. Zhang RR, Zhang YC, Pan L et al (2018) Engineering cobalt defects in cobalt oxide for highly efficient electrocatalytic oxygen evolution. ACS Catal 8(5):3803–3811
29. Zhang RR, Wang L, Pan L et al (2020) Solid-acid-mediated electronic structure regulation of electrocatalysts and scaling relation breaking of oxygen evolution reaction. Appl Catal B Environ 277:119237
30. Hu JN, Zhang XF, Xiao J et al (2021) Template-free synthesis of Co_3O_4 microtubes for enhanced oxygen evolution reaction. Chin J Catal 42(12):2275–2286
31. Kresse G, Furthmüller J (1996) Efficient iterative schemes for ab initio total-energy calculations using a plane-wave basis set. Phys Rev B Condens Matter 54(16):11169–11186
32. Perdew JP, Burke K, Ernzerhof M (1996) Generalized gradient approximation made simple. Phys Rev Lett 77(18):3865–3868
33. Kresse G, Joubert D (1999) From ultrasoft pseudopotentials to the projector augmented-wave method. Phys Rev B 59(3):1758–1775
34. Hashim AH, Zayed AOH, Zain SM et al (2018) Electronic, magnetic and structural properties of Co_3O_4 (100) surface: a DFT+U study. Appl Surf Sci 427:1090–1095
35. Wang CQ, Chen DR, Jiao XL (2009) Flower-like In_2O_3 nanostructures derived from novel precursor: synthesis, characterization, and formation mechanism. J Phys Chem C 113(18):7714–7718
36. Gulmine JV, Janissek PR, Heise HM et al (2002) Polyethylene characterization by FTIR. Polym Test 21(5):557–563
37. Chen YJ, Tian GH, Ren ZY et al (2011) Solvothermal synthesis, characterization, and formation mechanism of a single-layer anatase TiO_2 nanosheet with a porous structure. Eur J Inorg Chem 5:754–760
38. Jagadale AD, Kumbhar VS, Lokhande CD (2013) Supercapacitive activities of potentiodynamically deposited nanoflakes of cobalt oxide (Co_3O_4) thin film electrode. J Colloid Interface Sci 406:225–230
39. Wang WJ, Zhao Y, Zhang YG et al (2020) Defect-rich multishelled Fe-doped Co_3O_4 hollow microspheres with multiple spatial confinements to facilitate catalytic conversion of polysulfides for high-performance Li–S batteries. ACS Appl Mater Interfaces 12(11):12763–12773
40. Yuan D, Dou YH, Tian YH et al (2021) Robust pseudocapacitive sodium cation intercalation induced by cobalt vacancies at atomically thin $Co_{1-x}Se_2$/graphene heterostructure for sodium-ion batteries. Angew Chem Int Ed 60(34):18830–18837
41. Liu XM, Zhao LL, Xu HR et al (2020) Tunable cationic vacancies of cobalt oxides for efficient electrocatalysis in Li–O_2 batteries. Adv Energy Mater 10(40):2001415
42. Liu L, Jiang ZQ, Fang L et al (2017) Probing the crystal plane effect of Co_3O_4 for enhanced electrocatalytic performance toward efficient overall water splitting. ACS Appl Mater Interfaces 9(33):27736–27744
43. He D, Song XY, Li WQ et al (2020) Active electron density modulation of Co_3O_4-based catalysts enhances their oxygen evolution performance. Angew Chem Int Ed 59(17):6929–6935
44. Gao RJ, Wang J, Huang ZF et al (2021) Pt/Fe_2O_3 with Pt–Fe pair sites as a catalyst for oxygen reduction with ultralow Pt loading. Nat Energy 6(6):614–623
45. Zhou TT, Cao Z, Zhang P et al (2017) Transition metal ions regulated oxygen evolution reaction performance of Ni-based hydroxides hierarchical nanoarrays. Sci Rep 7:46154
46. Jović BM, Lačnjevac UČ, Jović VD et al (2015) Kinetics of the oxygen evolution reaction on NiSn electrodes in alkaline solutions. J Electroanal Chem 754:100–108
47. Lu JT, Wang SQ, Ding CF et al (2019) Metal organic frameworks derived $CoSe_2$@N-Doped-carbon-nanorods as highly efficient electrocatalysts for oxygen evolution reaction. J Alloys Compd 778:134–140
48. Pan JB, Wang BH, Wang JB et al (2021) Activity and stability boosting of an oxygen-vacancy-rich $BiVO_4$ photoanode by NiFe-MOFs thin layer for water oxidation. Angew Chem Int Ed Engl 60(3):1433–1440
49. Xie C, Yan DF, Li H et al (2020) Defect chemistry in heterogeneous catalysis: recognition, understanding, and utilization. ACS Catal 10(19):11082–11098
50. Sun SN, Li HY, Xu ZJ (2018) Impact of surface area in evaluation of catalyst activity. Joule 2(6):1024–1027

51. Zhang JM, Tao HB, Kuang M et al (2020) Advances in thermodynamic-kinetic model for analyzing the oxygen evolution reaction. ACS Catal 10(15):8597–8610
52. Ghosh KB, Zhang WY, Tassinari F et al (2019) Controlling chemical selectivity in electrocatalysis with chiral CuO-coated electrodes. J Phys Chem C 123(5):3024–3031
53. Shin Y, Kan WH, Aykol M et al (2018) Alleviating oxygen evolution from Li-excess oxide materials through theory-guided surface protection. Nat Commun 9(1):4597
54. Gracia J, Sharpe R, Munarriz J (2018) Principles determining the activity of magnetic oxides for electron transfer reactions. J Catal 361:331–338

Assoc. Prof. Lun Pan received his B.S. and Ph.D. degrees from the School of Chemical Engineering & Technology, Tianjin University, China, in 2009 and 2014, respectively. He was a visiting scholar in Georgia Institute of Technology from 2016 to 2017 and now he is an associate professor in Tianjin University. His research interests mainly focus on the design and synthesis of functional photocatalysts, their related modulation of morphology, facets, and surface defects, and their applications in photocatalysis, such as photocatalytic isomerization, hydrogen generation, and environmental remediation.

Prof. Ji-Jun Zou received his B.S., M.S., and Ph.D. degrees in chemical engineering from Tianjin University in 2000, 2002, and 2005, respectively. Then he became an assistant professor at School of Chemical Engineering and Technology, Tianjin University and was promoted as full professor from 2013. His research interests mainly surround nanostructured catalysts for photo/electrocatalysis, fuel processing, and biomass conversion. He has received several awards including Changjiang Scholar by MOE and Technological Leading Scholar of 10000 Talent project by MOST. He is also an associate editor of RSC Advances.